DEVELOPMENT OF A MECHANISTIC CRITICAL HEAT FLUX CORRELATION

Jeffrey Luitjens and Qiao Wu
Oregon State University
Department of Nuclear Engineering & Radiation Health Physics
3451 SW Jefferson Way; Corvallis, OR 97331
luitjenj@onid.oregonstate.edu; qiao.wu@oregonstate.edu

ABSTRACT

A mechanistic based critical heat flux (CHF) correlation has been developed derived from a mass, momentum, and energy balance at a nucleation site for water as the working fluid. The applicable range of the developed model is valid with inlet mass fluxes between 400 and $3,000\,kg/(m^2-s)$, pressures between 4.5 and 15.6 MPa, and critical qualities between -0.03 to 0.90. The resulting standard error of the mechanistic CHF model is 15% with over 800 experimental data points utilized over these conditions to inform and confirm the development of the model using a bundle geometry. Larger errors are obtained at conditions of low flow ($<400\,kg/(m^2-s)$), which is outside the determined applicable range of the proposed model. This behavior is expected due to the inherit two-phase instabilities at low-flow conditions and the potential of a different CHF mechanism occurring, such as that of the counter-current flow limiting (CCFL) CHF mechanism.

KEYWORDS
critical heat flux, CHF, DNBR, two-phase, boiling

1. INTRODUCTION

In industry the understanding of the limits of the boiling heat transfer mode is crucial to modeling the thermal hydraulic processes that occur to ensure the safe operation of industrial plants while enhancing a system's effectiveness; especially in nuclear power plants which are characterized by relatively high heat fluxes. At high heat fluxes a critical point is reached where the heat removal mechanisms are not sufficient enough to remove energy from the surface. This heat flux is referred to the critical heat flux (CHF). When the CHF point is reached the surface temperature rises due to the inability to remove the energy from the surface. This may result in temperatures often greater than the melting temperature of the surface. Understanding the heat transfer processes and the transitions involved is needed to appropriately model the mechanisms of the heat transfer modes to predict the onset of CHF to prevent such scenarios.

Currently, the mechanisms of boiling heat transfer and CHF are debated and not well understood and rely heavily on empirical correlations and lookup tables. This results in correlations that are often very specific to the scope of the developmental application; resulting from the lack of modeling of mechanistic behaviors. Modeling of the mechanistic process can result in a broader applicability of a developed model, as demonstrated here. Focus will be given to the development of a mechanist based critical heat flux correlation derived from a mass, momentum, and energy conservation equations.

The ability to develop a mechanistic based model allows for more confidence in the conceptual design phase of facilities that utilize high heat flux conditions. It also allows for the development for a more

mature correlation form. This has a significant effect on operating costs of high heat flux operating facilities in terms of margin management. A better understanding of one's limits with higher confidence allows for reduction in the potentially unnecessary margin that is used to account for any uncertainties in the utilized correlation. This reduction in margin allows for facilities to operate at a higher capacity increasing capital.

2. MECHANISTIC CHF MODEL DEVELOPEMENT

Derived will be the framework for determining a limiting surface heat flux for vertical flow boiling. This involves determining the separate heat transfer components that make up the total heat flux. Focus is given to the phenomena that occur very near the surface (scale of the bubble size). This approach is investigated by relating the forces acting on a bubble growing on a heated surface within a flow field. The limiting heat removal point (the critical heat flux) is hypothesized to occur at the highest attainable boiling frequency at a nucleation site given a nucleation site density over a heated surface. The highest attainable boiling frequency implies that at the same time a bubble departs from a nucleation site the next bubble immediately begins to grow. This model does not depend on the coalescence of departed bubbles away from the surface; rather it is postulated that the coalescence is a result of the large vapor generation from the highest attainable boiling frequency.

2.1. Heat Transfer Modes

The total surface heat flux can be partitioned into the following heat transfer modes:
- $q''_{1\phi}$ - convective heat flux
- q''_I - evaporation (interface) heat flux
- q''_{trans} - transient conduction heat flux
- q''_{slide} - sliding transient conduction heat flux

The total heat flux is expressed by Equation (1) with the mechanisms depicted in Figure 1.

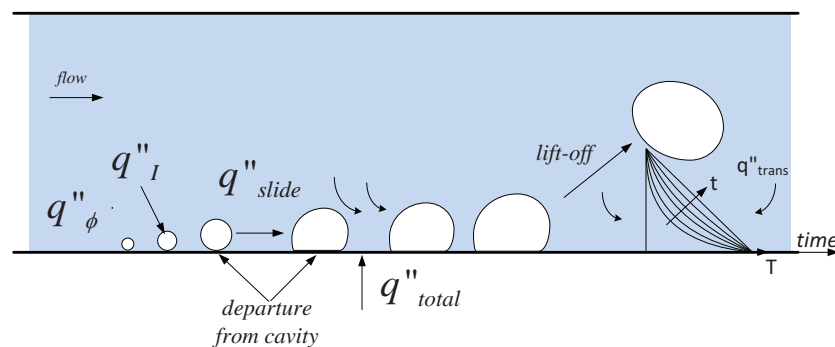$$q''_{total} = q''_{1\phi} + q''_I + q''_{trans} + q''_{slide} \tag{1}$$

Figure 1. Boiling heat transfer mechanisms at a heated surface.

It is assumed that the heat flux at the surface is high enough (due to the CHF condition) such that the bubble generation rate is continuous at a given nucleation site. This phenomenon was also considered by Zuber [1] where it was observed that as the surface heat flux increases the number of activated sites increases up to a point. Following a further increase in heat flux, resulted in an increase in the boiling frequency, not an increase in the number of activated sites. The number of sites only increases once a

continuous vapor column is formed. At this condition, the point of the potential limit of the nucleation site to remove energy has been reached.

Due to the high heat flux, the bubble departure from a cavity and bubble lift-off from the surface are assumed coincident (i.e. the bubble does not slide on the heated surface). This is assumed due to the initial rapid growth of the bubble causing the bubble to be ejected away from the surface with such a large force that any lateral drag that results from the flow conditions is overcome to prohibit much sliding of the bubble. This was also concluded by Victor et. al [2] in observance of their boiling data near the CHF condition (90%). Sliding is postulated to be more of a contributor to the low heat flux nucleate boiling process where the evaporation force and the lateral drag force are of a similar order of magnitude.

With these assumptions, liquid is not allowed to occupy the region of the previously departed bubble nor is there a lateral displacement of liquid along the surface where boiling does not occur due to the prohibition of bubble sliding. Thus, the transient conduction heat flux mechanism at the nucleation site and heat removal from sliding of a bubble along the surface are neglected from Equation (2). The two major contributions to the total heat flux is expressed by Equation (3).

$$q''_{total} = q''_{1\phi} + q''_I + q''_{trans} + q''_{slide} \tag{2}$$

$$q''_{total} = q''_{1\phi} + q''_I \tag{3}$$

Relations describing the evaporative interfacial energy transfer (q''_I) and the single phase heat transfer ($q''_{1\phi}$) are developed in the following sections.

2.2. Bubble Forces Perpendicular to a Vertical Heated Surface

An extensive review of the forces acting on a growing bubble is provided by Thorncroft [3, 4] for various boiling configurations. A similar force balance as that employed here was performed by Kandlikar [5] in the investigation of orientation effects on the CHF condition. For a vertically aligned flow channel the assumed significant forces acting perpendicular to a heated surface are the: surface tension force (F_σ), evaporative thrust force (F_{evap}), and the bubble shear lift force (F_{sL}). These forces are depicted in Figure 2.

The forces in action on a single bubble are described in the following sub-sections. For this analysis only the forces perpendicular to the heated surface are assumed to participate in the departure of the bubble. The buoyancy force is neglected since it is assumed to be negligible when compared to the evaporative thrust force. This is due to being near the CHF condition (i.e. large heat fluxes and evaporation rates). The lateral drag force (in the direction of flow) on a bubble is also neglected here based on the assumption this force is small relative to the assumed acting forces. Both these forces work to remove the bubble from the surface.
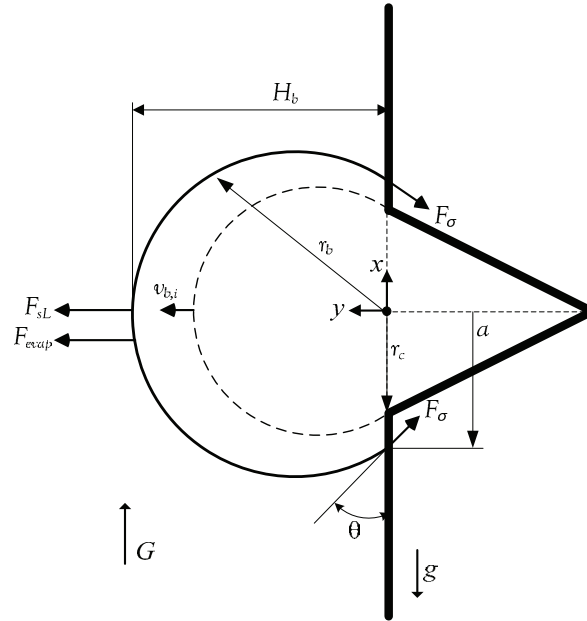
Figure 2. Spherical bubble perpendicular force balance on a vertically aligned heated surface.

2.2.1. Surface Tension Force (F_σ)

The surface tension force describes the force along the bubble interface contact line with the surface. This forces works to keep the bubble interface attached to the surface and is expressed by Equation (4).

$$
\begin{aligned}
F_{\sigma,y} &= 2\pi\sigma a sin(\theta) \\
\sigma &= \text{surface tension} \\
a &= \text{radius of vapor and solid contact area} \\
\theta &= \text{liquid-vapor-solid interface contact angle}
\end{aligned}
\tag{4}
$$

Here the static contact angle will be used (not the receding or advancing contact angle) resulting in an equal and opposite horizontal surface tension force.

2.2.2. Evaporative Thrust Force (F_{evavp})

The evaporative thrust derives from the bubble growth rate due to the interfacial mass/energy transfer across the bubble interface. This force is identical to that of the thrust force that results by mass discharge across a nozzle boundary and is depicted in Figure 3. The difference here, when compared to a nozzle which has a constant plane area at which this force acts, is that the area of action (bubble interface area) is dynamic.
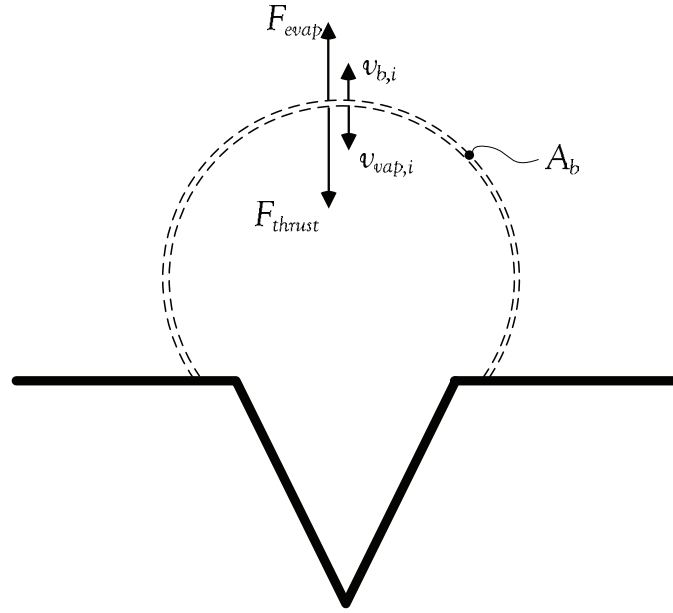
Figure 3. Evaporative thrust force due to mass/energy exchange across a bubble interface.

This evaporative force will be shown to be proportional to the square of the heat flux and the bubble size (interfacial area). Due to symmetry, the thrust forces in the direction parallel to the heated surface negate each other. In the direction perpendicular to the surface there is a net reaction force (F_{evap}) causing the bubble interface to displace away from the heated surface due to mass/energy exchange across the bubble interface area. The net evaporative force is defined by Equation (5).

$$-F_{thrust} = F_{evap} = \frac{d(mv)}{dt} = v\frac{\partial m}{\partial t} + m\frac{\partial v}{\partial t} \tag{5}$$

The surface velocity perpendicular to the heated surface is determined by an energy balance of the growing bubble. The bubble here is assumed to have a spherical shape as shown in Figure 2. An energy balance of the bubble (Equation (6)) relates the bubble size to the heat transfer across the bubble interface.

$$\rho_v h_{fg}\frac{dV_b}{dt} = q_I'' A_b \tag{6}$$

The terms q_I'' and A_b of Equation (6) represent the heat transfer rate at the bubble interface and the total bubble interface surface area. The volume and surface area of a spherical shaped bubble are defined by Equation (7).

$$V_b = \frac{\pi}{6}H_b\left(3a^2 + H_b^2\right), \qquad A_b = 2\pi r_b H_b = \pi\left(a^2 + H_b^2\right) \tag{7}$$

Here a is the vapor-solid contact radius and H_b is the bubble height from the surface to the bubble cap, both of which vary with time as the bubble grows. Inserting these geometric relations into Equation (6), the bubble interface velocity perpendicular to the heated surface can then be expressed by Equation (8).

$$v_{b,i} = \frac{dH_b}{dt} = \frac{2q_{i''}}{\rho_v h_{fg}} \tag{8}$$

It is noted that the interface velocity is independent with time with the assumption that the interfacial heat flux is also constant with time. The mass evaporation rate at the interface is found similarly using the energy balance equation and is expressed as Equation (9).

$$\dot{m}_b = \frac{dm_b}{dt} = \frac{q_{i''}\pi\left(a^2 + H_b^2\right)}{h_{fg}}. \tag{9}$$

Inserting Equation (8) and Equation (9) into Equation (5) and noting that since the rate of change of the bubble height is constant (constant interface velocity) the evaporative thrust force is then expressed by Equation (10).

$$F_{evap} = v_{b,i}\frac{dm_b}{dt} = \left(\frac{q_{i''}}{h_{fg}}\right)^2 \frac{\pi\left(a^2 + H_b^2\right)}{\rho_v} \tag{10}$$

2.2.3. Bubble Shear Lift Force (F_{sL})

The bubble shear lift force results from the entrainment phenomena on a bubble from the bulk fluid movement parallel to the surface. The result of such a force is to aid in bubble removal from the surface and will thus result in a decrease in the maximum heat flux required to remove a bubble. With the increase of this force the evaporative potential will decrease but there will be a counter increase in the convective heat flux due to the bulk velocity dependence. The lift force as derived by Klausner and Mei [6] is expressed in a general form by Equation (11).

$$F_{sL} = \frac{1}{2}C_L\rho_l u_l(y')^2 \pi r_b^2 \tag{11}$$

Where y' is the bubble center of mass distance from the wall approximated here as $y' \approx H_b/2$. The lift coefficient is expressed by Equation (12) with G_s and the bubble Reynolds number (Re_b) defined by Equation (13).

$$C_L = 3.877G_s^{\frac{1}{2}}\left[Re_b^{-2} + 0.014003G_s^2\right]^{\frac{1}{4}} \tag{12}$$

$$G_s = \left|\frac{du_l}{dy}\right|\frac{y}{u_l(y)}, \quad Re_b = \frac{r_b u_l(y')}{\nu_l} \tag{13}$$

Using the standard turbulence definitions, the non-dimensional velocity and distance from the wall are expressed by Equation (14).

$$u^+ = \frac{u_l}{u^*} = \frac{u_l}{\sqrt{\tau_w / \rho_l}}, \quad y^+ = \frac{yu^*}{\nu_l} = \frac{y\sqrt{\tau_w / \rho_l}}{\nu_l} \tag{14}$$

The bubbles are assumed to be of a small size such that the distance from the center of a bubble to the wall is assumed to be small with a $y^+ \leq 5$. This allows for approximating y^+ and u^+ as being equal (Equation (15)).

$$y^+ = u^+. \tag{15}$$

The wall shear stress is determined by Equation (16) with the defined moody friction coefficient of Equation (17). U_l is the volumetric average velocity.

$$\tau_w = C_f \frac{1}{2} \rho_l U_l^2, \; C_f = \frac{\lambda}{4} \tag{16}$$

$$\lambda = \begin{cases} \dfrac{64}{Re}, & Re < 2320 \\ \dfrac{0.3164}{Re^{0.25}}, & 4x10^3 < Re < 10^5 \\ 0.0032 + 0.221Re^{-0.237}, & 10^5 < Re < 2x10^6 \end{cases} \tag{17}$$

The differential term of Equation (13) is evaluated with Equation (14) and expressed by Equation (18).

$$\left| \frac{du_l}{dx} \right| = \frac{u^{*2}}{\nu_l} \left| \frac{du^+}{dx^+} \right|. \tag{18}$$

Based on Equation (15) and Equation (18), the expression for G_s simplifies to 1.0 as shown by Equation (19).

$$G_s = \left| \frac{du_l}{dx} \right| \frac{y}{u_l(y)} = \frac{\tau_w}{\mu_l} \frac{y}{\dfrac{\tau_w}{\mu_l} y} = 1.0. \tag{19}$$

With the derived relations above, the shear lift force induced on a growing bubble by a flow parallel to the surface can be determined by the general expression given by Equation (11).

2.3. Critical Heat Flux Model

The balance equation for the final forces considered is expressed by Equation (20). Substituting the force expressions from the previous sections, the general force balance for a bubble is expressed by Equation (21) where the end point of bubble growth is then taken to be the time at which the forces are balanced. That is $dM/dt = 0$.

$$\frac{dM}{dt} = -F_{\sigma,y} + F_{evap} + F_{sL} \tag{20}$$

$$0 = -2\pi\sigma a\sin(\theta) + \left(\frac{q_I''}{h_{fg}}\right)^2 \frac{\pi\left(a^2 + H_b^2\right)}{\rho_v} + \frac{1}{2}C_L\rho_l u_l \big|_{H/2}^2 \pi r_b^2 \tag{21}$$

Solving for the interfacial heat flux (q_I''), the evaporative component of the heat flux is finally expressed by Equation (22).

$$q_I'' = \left(\left|\frac{2\pi\sigma a\sin(\theta) - \frac{1}{2}C_L\rho_l u_l\big|_{H/2}^2 \pi r_b^2}{\dfrac{\pi\left(a^2 + H_b^2\right)}{\rho_v h_{fg}^2}}\right|\right)^{1/2} \tag{22}$$

This provides the evaporative heat flux component of Equation (3). The fractional boiling area of Equation (23) is determined from the nucleation site area density (Na), the average bubble size ($\overline{A}_b$), and the total heated area (A_h). The total contribution to the convective heat flux is then the complement of Equation (23).

$$f_{boil} = NaA_h \frac{\overline{A}_b}{A_h} = Na\overline{A}_b \tag{23}$$

With the evaporative and convective heat flux components defined, the total heat transfer is then described by Equation (24).

$$q_{total}'' = \overline{h}_{conv}\left(T_w - T_{bulk}\right)(1 - f_{boil}) + \left(\left|\frac{2\pi\sigma a\sin(\theta) - \frac{1}{2}C_L\rho_l u_l\big|_{H/2}^2 \pi r_b^2}{\dfrac{\pi\left(a^2 + H_b^2\right)}{\rho_v h_{fg}^2}}\right|\right)^{1/2} f_{boil} \tag{24}$$

This equation is used to postulate the maximum potential heat transfer for flow boiling. The step by step process for solving Equation (24) is provided below. The theoretically derived critical heat flux value is to be solved axially in a flow channel. This is then compared to experimental data to validate the newly developed mechanistic model that is derived from a mass, momentum, and energy balance of a bubble at a nucleation site. The solution steps are as follows:

1. Specify specific channel geometry.
2. Specify fluid boundary conditions (system pressure, inlet mass flux, inlet temperature/enthalpy)
3. Define resolution of axial nodalization.
4. Define the heat flux profile to test.
5. Solve the one-dimensional energy equation to determine the axial dependent fluid properties at each axial node.
6. The effective active cavity size is then determined with the calibration curve (Section 2.4.1) dependent on the heated surface conditions, system pressure and mass flux.

7. Based on effective active cavity size the wall temperature is approximated with the Clausius-Claperyeon relationship.
8. The boiling suppression (S) factor is calculated to determine effective wall temperature.
9. Solve for near wall thermal fluid properties with effective wall temperature.
10. The contact angle is defined based on the test fluid and surface.
11. With a spherical bubble shape, contact angle, and effective cavity size the bubble interfacial area is calculated.
12. The nucleation site density is calculated based on wall superheat and contact angle.
13. The surface boiling fraction and the convective fraction is determined based on nucleation site density.
14. The individual terms of the force balance equation are solved and the maximum boiling heat flux calculated.
15. The single phase convective heat flux is calculated.
16. The boiling and convective heat fluxes are than partitioned based on the available boiling and convective fractional areas.
17. The sum of the partitioned boiling and convective heat flux is taken to be the predicted critical heat flux and is obtained for each axial node.

The remaining closure relations to be defined are the: effective nucleation site cavity size, bubble-surface contact angle, bubble-surface contact radius, effective wall heat (suppression (S) factor) for nucleate boiling, nucleation site density to partition the convective and boiling heat fluxes, and convective heat flux correlation. The choice and justification for each constitutive relation is described in the following section.

2.4. Critical Heat Flux Model Constitutive Relations

2.4.1. Effective Nucleation Site Cavity Radius

This parameter is the calibration coefficient for the model. The effective nucleating cavity size is determined by calibrating a single set of data for a given geometric condition and surface type/finish. The effective nucleation site size is dependent on the local surface conditions. Specifically, it is dependent on the wall superheat temperature (related to the physical surface characteristics) and the boundary layer profile.

The wall superheat represents the maximum temperature a nucleating bubble can reach before heat transfer ceases. The maximum temperature limit defines the maximum internal saturation pressure of the bubble. With the maximum internal pressure determined the limit for the smallest supported bubble size can be quantified. This is demonstrated with the use of the Clausius-Clapeyron relation of Equation (25).

$$D = \frac{4\sigma T_{sat}}{\left(T_v - T_l\right)\Delta h_{fg}\rho_\nu}. \tag{25}$$

The thermal boundary layer presents another limit for bubble growth. If the bubble grows beyond the point in the thermal boundary where the boundary layer temperature is equal to the bubble internal temperature a secondary path for heat rejection exists (condensation at the bubble cap). This will limit the bubble growth rate and size.

To account for these two effects, two independent variables are chosen to represent the effective cavity size in a functional form. These parameters are system pressure and inlet mass flow rate. It is noted that

mass flow rate could be replaced by velocity, mass flux, Reynolds number, non-dimensional velocity, etc., just as long as velocity is represented.

2.4.2. Bubble Contact Angle

A representative static contact angle of $45.0°$ is assumed. This is applicable for copper and stainless steel surfaces over a broad range of surface roughnesses. It is believed that the lack modeling of the exact value will be captured within the nucleation site size calibration. A more complex relation of contact angle could be employed if desired. The effects of dynamic versus receding contact angles are not taken into account here.

2.4.3. Bubble Contact Radius

The bubble-surface contact radius (a) as depicted in Figure 2 needs yet to be determined for use in Equation (24). The contact radius is defined as to obtain the maximum theoretical potential heat flux with the use of Equation (22). It can be shown that when the contact area between bubble vapor region and the surface is the smallest the value of the interfacial heat flux is the largest. It is further assumed that the bubble contact radius can be no smaller the cavity size. The cavity size is thus taken to be the bubble-surface contact radius. This implies that once a bubble completely emerges from a cavity it is ejected from the surface and no longer allowed to grow. This assumption is consistent with the high boiling frequencies and high heat fluxes that exist at/near the CHF condition.

2.4.4. Nucleation Site Density

The nucleation site density as a function of wall superheat was fit by Basu [7] based on experimental data. Most data was correlated to within 40%. This relation is used in Equation (23) to determine the boiling fraction of the entire heated surface area.

$$
\begin{aligned}
N_a &= 0.34\left(1 - cos(\theta_s)\right)\Delta T_w^{2.0} && \Delta T_w < 15° \\
N_a &= 3.4x10^{-5}\left(1 - cos(\theta_s)\right)\Delta T_w^{5.3} && \Delta T_w \geq 15° \\
&\quad with, \\
N_a &= \text{nucleation site density } \left[sites\,/\,cm^2\right] \\
\theta_s &= \text{static contact angle}\left[degrees\right] \\
\Delta T_w &= \text{wall superheat temperature } [°C\ ]
\end{aligned}
\tag{26}
$$

2.4.5. Convective Heat Flux Correlation and Boiling Suppression

The convective heat correlation used is the Dittus-Boelter relation as written in Equation (27).

$$
h_{mac} = 0.023 \text{Re}^{0.8}\text{Pr}^{0.4}\left(\frac{\text{k}}{\text{D}}\right)
\tag{27}
$$

The boiling suppression factor developed by Chen [8] is used to determine the effect wall superheat. The wall superheat determines the near wall fluid properties.

3. CHF TEST DATA

Columbia University compiled an extensive database of over 11,000 data points for 235 different test section assemblies for the EPRI CHF correlation development [9-12]. The data from the General Electric test series (test sections 301-318) are used as the focus for the model development here. A total of 871 data points were collected for this test series. All test sections have the same geometry with all test configurations utilizing a uniform power profile with varying radial peaking factors. The test series consisted of the following test ranges: inlet mass fluxes 305 to $4,300\,kg\,/\,(m^2 - s)$, pressures 4.0 to 15.6 MPa, and critical qualities -0.03 to 1.0. The CHF pin and peaking factor from the experiment was taken to be the pin model applied to the model.

The range of the applicability of the proposed model is considered to be with an inlet mass fluxes between 400 to $3,000\,kg\,/\left(m^2 - s\right)$, pressures 4.5 to 15.6 MPa, and critical qualities between -0.03 to 0.90. It is noted that the empirical EPRI CHF correlation developed was determined to also be applicable only above the 400 $kg\,/\left(m^2 - s\right)$ mass flux range.

4. CHF CORRELATION RESULTS

The proposed model and solution algorithm are coded using MATLAB© version 2014b. The following sections will discuss the implementation and results of the model compared to the EPRI experimental data presented in Section 3.

4.1. Model Nodalization

A one-dimensional axial nodalization is defined with three sub-regions. The first region is the wall heat source modeled as a heat flux boundary condition. The second is the fluid near the wall with fluid properties determined at the wall temperature. This region is modeled as having zero thickness. The last region is the bulk region where fluid properties are determined by a one-dimensional energy balance in the axial direction of the channel. Figure 4 depicts the nodalization scheme and the three sub-regions.
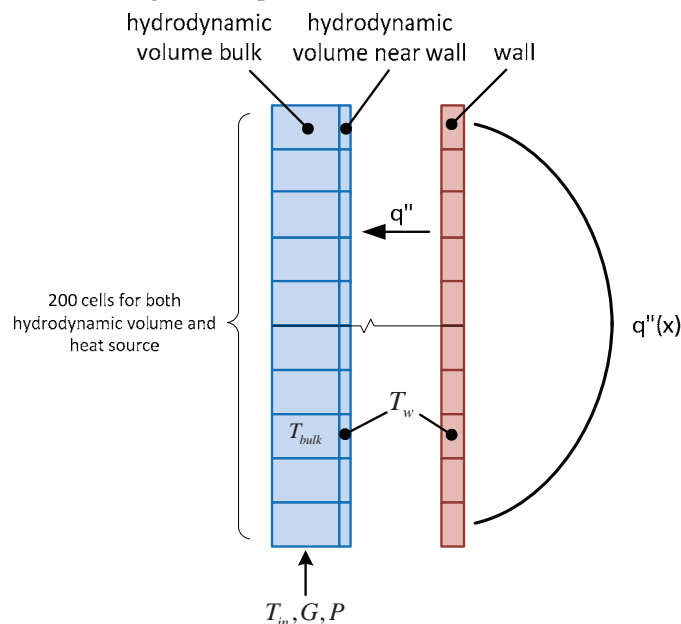

Figure 4. Axial nodalization of critical heat flux subchannel model.

4.2. Model Calibration

Based on the data collected by Columbia University for the EPRI CHF database (Section 3) a calibration was performed as discussed in Section 2.4.1 to determine the effective active nucleation site cavity size. Dependence was found to be mainly related to the system pressure and mass flux (velocity) with the relation defined by Equation (28) relating the effective nucleation cavity size (r_c) in microns to the system pressure (P_{sys}) in bars and inlet mass flux (G) in $kg/(m^2-s)$. It is noted that although five coefficients are defined in Equation (28), not all coefficients are necessary, dependent on the overall order of magnitude of each term.

$$
\begin{aligned}
r_c\left[microns\right] \quad &= a_0 + a_1 G + a_2 P_{sys} + a_3 G^2 + a_4 G P_{sys} + a_5 P_{sys}^2 \\
a_0 &= 0.293 \qquad a_1 = -3.133 x 10^{-5} \\
a_2 &= -1.805 x 10^{-3} \quad a_3 = 4.258 x 10^{-9} \\
a_4 &= 1.022 x 10^{-8} \qquad a_5 = 3.264 x 10^{-6}
\end{aligned}
\tag{28}
$$

4.3. Critical Heat Flux Value

When looking at the full tested parameter range for EPRI test 301-318, a grouping is observed in left image of Figure 5 where poor performance occurs. This large error grouping corresponds to conditions where the mass flux is less than $400\,kg/(m^2-s)$ and is believed to be the result of a different CHF mechanism occurring to initiate the onset of the CHF condition. Typically during CHF testing the channel mass flux is controlled by throttling an inlet valve. At low mass fluxes so much throttling is believed to occur that the channel becomes starved of the necessary inventory needed to replace the boiling liquid in the channel. This is synonymous to the counter-current flow limiting (CCFL) CHF mechanism. This behavior is contrary to the pool boiling condition where an infinite replenishment inventory is available; this is the condition assumed by this model. It is typical for pool boiling CHF models to over-predict CHF occurring under CCFL conditions.

The right image of Figure 5 presents only the data that is applicable to the range of development for the proposed model. As can be seen good agreement is obtained between the model and data with the exception of EPRI test 304 where a consistent deviation in the 30%-40% range exists. The distribution of error is presented in Figure 6 and as can be seen a normal distribution is obtained with a standard error of 15%.
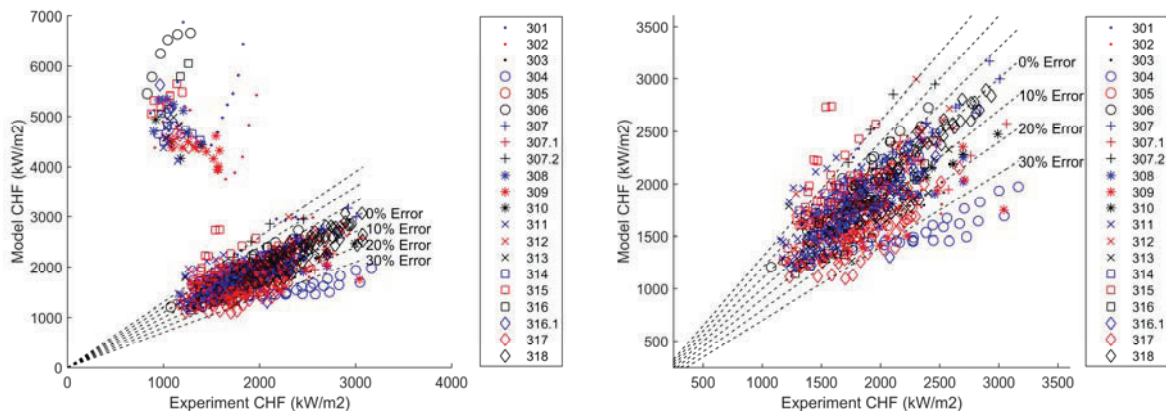

Figure 5. Model CHF performance compared to full (left) and applicable (right) test parameters from EPRI database tests 301-318.
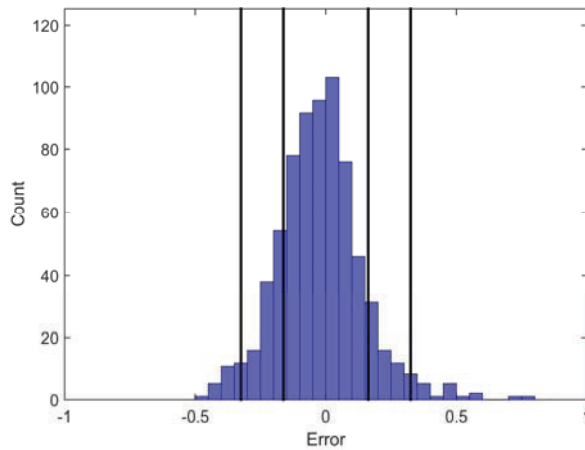
Figure 6. Model CHF error for applicable data set range; σ=0.15.

4.4. Correlation Bias

The correlation bias is investigated by comparing the calculated error to various model parameters. Here bias is defined by a distinct upward/positive or downward/negative shift in the error as a function of the magnitude of the observed parameter. This is done to ensure there are no biased dependencies/drift in correlation results due to model parameters. As observed by the results no apparent bias exists and demonstrates that the relative importance of each parameter is correctly captured.
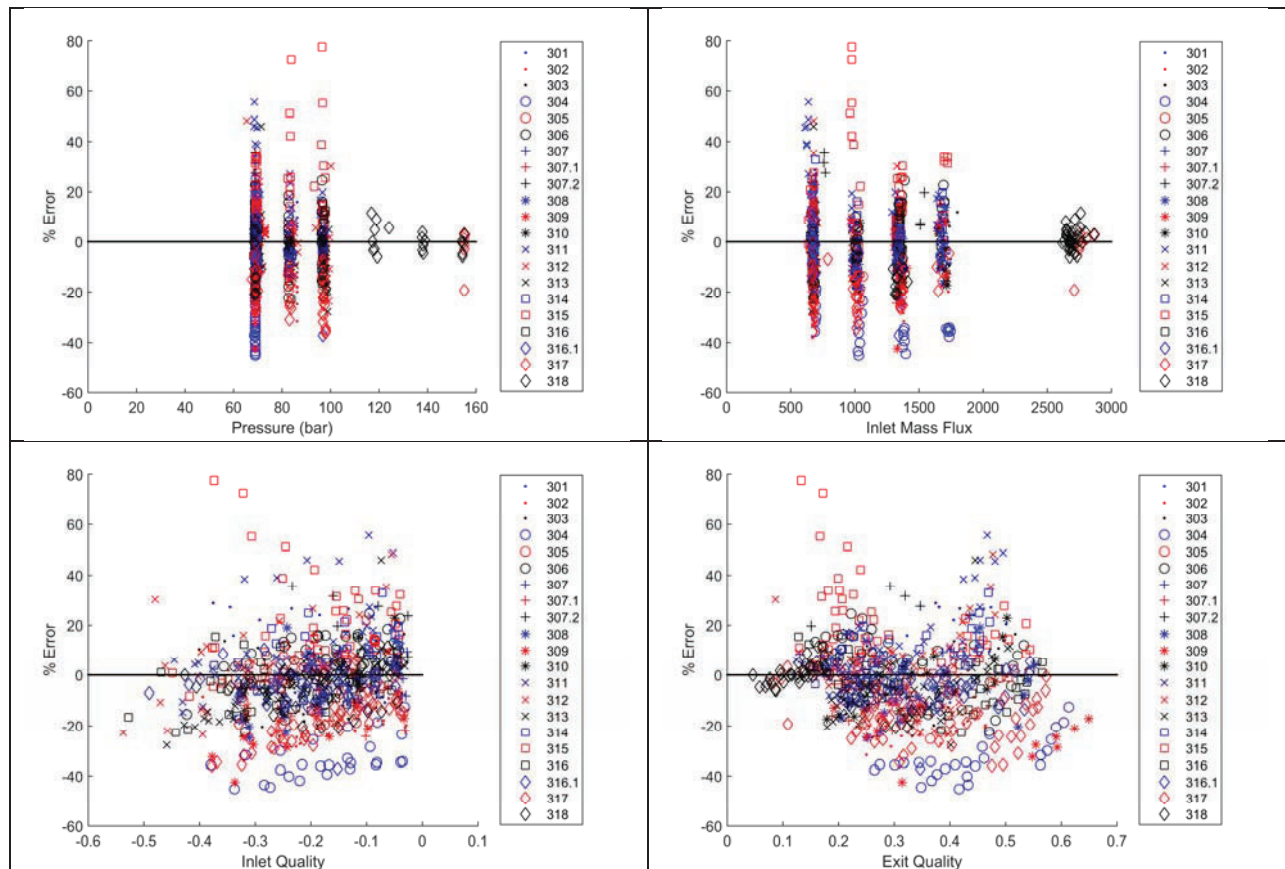

Figure 7. Correlation bias for pressure, inlet mass flux, inlet quality, and critical quality.

5. CONCLUSIONS

A mechanistic based CHF correlation has been developed derived from a mass, momentum, and energy balance at a nucleation site. The applicable rang of the developed is valid with inlet mass fluxes between 400 and $3,000\, kg/(m^2-s)$, pressures between 4.5 and 15.6 MPa, and critical qualities between -0.03 and 0.90. The resulting standard error of the CHF model is 15% with a sample of over 800 CHF data points.

6. ACKNOWLEDGMENTS

7. REFERENCES

1. Zuber, N., *Hydrodynamic Aspects of Boiling Heat Transfer*. 1959.
2. Victor, H., M. Del Valle, and D.B.R. Kenning, *Subcooled flow boiling at high heat flux*. International Journal of Heat and Mass Transfer, 1985. **28**: p. 1907-1920.
3. Thorncroft, G.E., J.F. Klausner, and R. Mei, *An experimental investigation of bubble growth and detachment in vertical upflow and downflow boiling*. International Journal of Heat and Mass Transfer, 1998. **41**(23): p. 3857-3871.
4. Thorncroft, G.E., *Bubble Forces and Detachment Models*. Multiphase Science and Technology, 2001. **13**(3): p. 35-76.
5. Kandlikar, S.G., *A Theoretical Model to Predict Pool Boiling CHF Incorporating Effects of Contact Angle and Orientation*. Journal of Heat Transfer, 2001. **123**(6): p. 1071.
6. Klausner, J.F., et al., *Vapor Bubble Departure in Forced-Convection Boiling*. International Journal of Heat and Mass Transfer, 1993. **36**(3): p. 651-662.
7. Basu, N., G.R. Warrier, and V.K. Dhir, *Onset of Nucleate Boiling and Active Nucleation Site Density During Subcooled Flow Boiling*. Journal of Heat Transfer, 2002. **124**(4): p. 717-728.
8. Chen, J.C., *Correlation for Boiling Heat Transfer to Saturated Fluids in Convective Flow*. Industrial and Engineering Chemistry Process Design and Development, 1966. **5**(3): p. 322-329.
9. Fighetti, C.F. and D.G. Reddy, *Parametric Study of CHF Data, Volume 1: Compilation of Rod Bundle CHF Data Available at the Columbia University Heat Transfer Research Facility*, E.P.R.I. (EPRI), Editor. 1982.
10. Fighetti, C.F. and D.G. Reddy, *Parametric Study of CHF Data, Volume 2: A Generalized CHF Correlation*, E.P.R.I. (EPRI), Editor. 1982.
11. Fighetti, C.F. and D.G. Reddy, *Parametric Study of CHF Data, Volume 3 Part 1: Critical Heat Flux Data*, E.P.R.I. (EPRI), Editor. 1982.
12. Fighetti, C.F. and D.G. Reddy, *Parametric Study of CHF Data, Volume 3 Part 2: Critical Heat Flux Data*, E.P.R.I. (EPRI), Editor. 1982.